



Cite this: *RSC Adv.*, 2020, 10, 34702

# Construction of Ag-modified TiO<sub>2</sub>/ZnO heterojunction nanotree arrays with superior photocatalytic and photoelectrochemical properties

Kang Xu,  Zhu Liu, Shihan Qi, Zhuangzhuang Yin, Shangkun Deng, Miao Zhang and Zhaoqi Sun\*

The work involves the preparation of TiO<sub>2</sub>/ZnO heterojunction nanotree arrays by a three-step: hydrothermal, sol-gel, and secondary hydrothermal method, and then modification of Ag quantum dots (QDs). In the above process, the ZnO nanoparticles attached to the TiO<sub>2</sub> surface were subjected to secondary growth by a hydrothermal method to form a unique nanotree structure with TiO<sub>2</sub>, followed by Ag quantum dot modification by quantum dot deposition. In summary, TiO<sub>2</sub>/ZnO nanotree arrays are cited for the first time. The prepared Ag-modified TiO<sub>2</sub>/ZnO heterojunction nanotree arrays were found to exhibit enhanced photoelectrochemical and photocatalytic properties. The photocurrent of the Ag-modified TiO<sub>2</sub>/ZnO heterojunction nanotree arrays is increased by 8-fold compared to the pure TiO<sub>2</sub> nanorod arrays, the photocatalytic degradation rate within 180 minutes increased from 37% to 77% and the kinetic rate constants for the degradation of methyl orange were three times higher than the pure TiO<sub>2</sub> nanorod arrays. The improved performance is partly due to the introduction of the TiO<sub>2</sub>/ZnO heterojunction nanotree arrays which provide Ag QDs with greater adhesion area. Localized surface plasmon resonance (LSPR) leads to an increase in the intensity of absorbed light due to the modification of Ag QDs. On the other hand the generation of the TiO<sub>2</sub>/ZnO heterojunction decreases the forbidden band width, resulting in the redshift of the light absorption edge. Therefore, TiO<sub>2</sub>/ZnO heterojunction nanotree arrays are expected to play an important role in solar cells and photocatalytic materials.

Received 30th July 2020  
Accepted 10th September 2020

DOI: 10.1039/d0ra06596j

rsc.li/rsc-advances

## 1. Introduction

Semiconductor oxides comprise a class of compounds with unique optical and electrical properties. Many semiconductor oxides have been found to be ideal photocatalysts for the decomposition of organics.<sup>1,2</sup> However related reports show that in a single semiconductor, the recombination of electron-hole pairs occurs very rapidly, which significantly reduces the photocatalytic efficiency of these materials and makes them difficult to use.<sup>3-6</sup> For nearly a decade, in order to increase photocatalytic activity by promoting the separation of photo-excited charges or improving the surface of photocatalysts, various strategies have been employed. For example, suitable structural designs, ion doping, and the formation of semiconductor heterojunctions by combining with metals or other semiconductors.<sup>7-11</sup> Among them, the construction of semiconductor heterojunctions has attracted much attention due to their significant improvement in photocatalytic activity.<sup>12,13</sup>

TiO<sub>2</sub> and ZnO have been proved to be the best photocatalysts for the oxidative degradation of organic compounds in many semiconductor oxides under ultraviolet (UV) irradiation. TiO<sub>2</sub> is the most widely used semiconductor photocatalytic material due to its suitable band structure (3.2 eV), stable chemical properties, high corrosion resistance, non-toxic and low cost.<sup>14-18</sup> ZnO (3.37 eV) and TiO<sub>2</sub> have similar band gaps. The higher electron mobility enable ZnO to exhibit a higher photocatalytic efficiency than TiO<sub>2</sub>. Moreover, the unique electrical and optical properties of ZnO make it promising for applications in photocatalysis. However, ZnO is less stable than TiO<sub>2</sub> (which is more prone to photocorrosion), which severely limits the use of ZnO. The combination of TiO<sub>2</sub> and ZnO can give an oxide mixed heterostructure having good photocatalytic properties.<sup>19,20</sup> As a result, the TiO<sub>2</sub>/ZnO heterostructure has also been extensively studied. For instance, Wang *et al.* applied TiO<sub>2</sub> to the surface of ZnO and observed that the charge recombination was inhibited and UV absorption was increased compared to bare TiO<sub>2</sub>.<sup>21</sup> Furthermore, Johra *et al.* found that the TiO<sub>2</sub>/ZnO heterojunction was better than that of ZnO alone.<sup>22</sup> The coupled synergistic effect of the metal oxide TiO<sub>2</sub> and ZnO can change their electronic state to produce

School of Physics & Materials Science, Anhui University, Hefei 230601, PR China.  
E-mail: szq@ahu.edu.cn



photogenerated charge carriers that facilitate the separation of the electron pairs.<sup>23</sup> As a result, the electrons are transferred from the conduction band (CB) of ZnO to the CB of TiO<sub>2</sub>,<sup>24</sup> likewise, holes can be transferred from the valence band (VB) of TiO<sub>2</sub> to VB of ZnO.<sup>23</sup> The heterostructure simultaneously accelerates the decrease in the electron-hole pair recombination in the semiconductor and increases the lifetime of carriers.<sup>25</sup> Although TiO<sub>2</sub>/ZnO heterostructures can impede the recombination of electron-hole pair, there are also many disadvantages, such as poor response of visible light and high photocorrosion. Metal quantum dots (QDs) own premium optical characteristics, involving adjustable bandgap, high extinction coefficient, and optical absorption range.<sup>26–28</sup> Among metal quantum dots, Ag QDs have attracted more and more attention because of their longitude surface plasmon resonance (LSPR) and show the best photocatalytic properties in semiconductor heterojunctions.<sup>29,30</sup>

According to the advantages of Ag QDs of TiO<sub>2</sub>/ZnO heterojunction, in order to better improve photoelectrochemical performance and photocatalytic performance, ZnO nanorods were grown on TiO<sub>2</sub> nanorods by hydrothermal method to form TiO<sub>2</sub>/ZnO heterojunction nanotree arrays, then modify TiO<sub>2</sub>/ZnO heterojunction nanotree arrays with Ag QDs (Scheme 1). The photocatalytic properties and photoelectrochemical of the samples were tested. It was found that Ag-modified TiO<sub>2</sub>/ZnO nano-dendritic heterostructures have enhanced photoelectrochemical and photocatalytic properties.

## 2. Experimental

### 2.1 TiO<sub>2</sub>/ZnO heterojunction nanotree arrays preparation

TiO<sub>2</sub> nanorod arrays was directly synthesized by a simple hydrothermal method. The tetrabutyl butoxide (C<sub>16</sub>H<sub>36</sub>O<sub>4</sub>Ti, CP), deionized water (DIW) and hydrochloric acid (HCl) were

mixed in the ratio of 1 : 30 : 30 to obtain a culture solution, the FTO conductive glass was placed in an autoclave, and the culture solution was added to immerse the conductive glass. Then, after 12 hours of reaction at 150 °C, cool to room temperature, rinse with deionized water and absolute ethanol, and dry to obtain a transparent fluoride-doped tin oxide (FTO) conductive glasses with TiO<sub>2</sub> nanorods arrays on its surface.

The ZnO seed layer was first prepared by the sol-gel method. 0.4 mol of zinc acetate dihydrate (Zn(CH<sub>3</sub>COO)<sub>2</sub>·2H<sub>2</sub>O) was dissolved in 100 mL of ethylene glycol monomethylether (HOCH<sub>2</sub>CH<sub>2</sub>OCH<sub>3</sub>), magnetically stirred for 10 min at 60 °C, and then diethanolamine (C<sub>4</sub>H<sub>11</sub>NO<sub>2</sub>) having a concentration of Zn<sup>2+</sup> or the like was added dropwise as a stabilizer to the solution and continued stirring for 30 min to obtain Zn<sup>2+</sup> seed solution at a concentration of 0.4 mol L<sup>-1</sup>. Preparation of ZnO

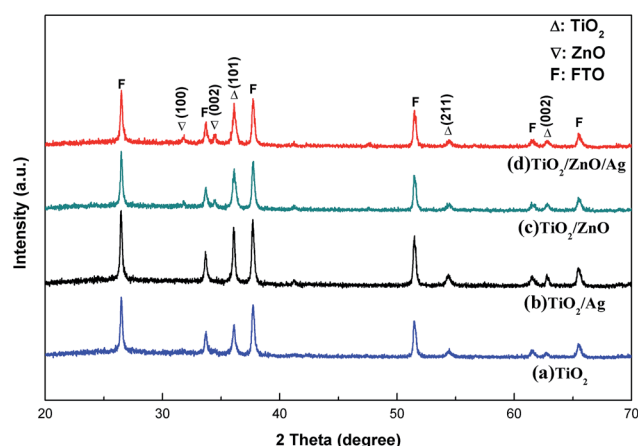
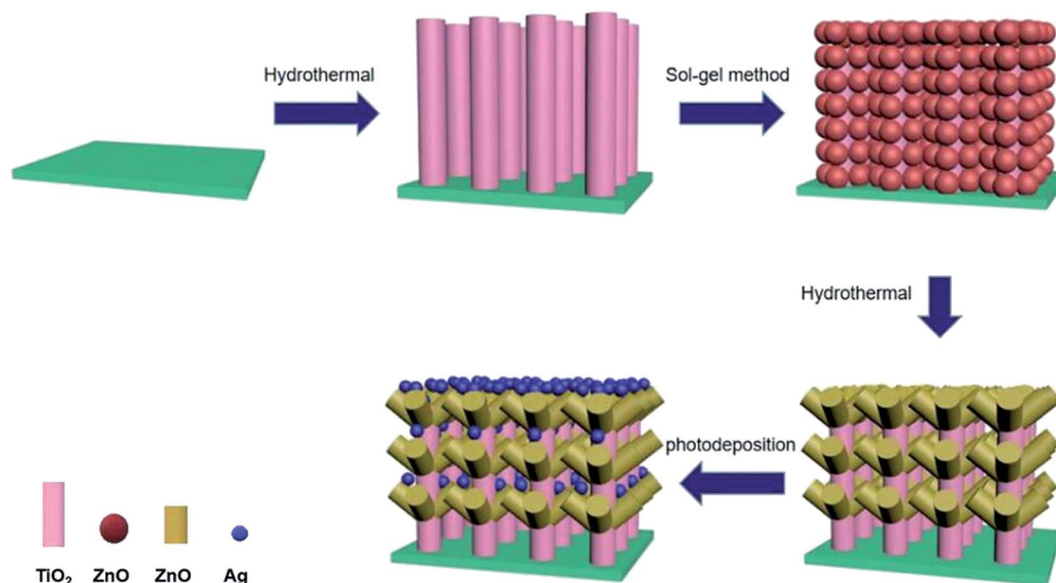


Fig. 1 XRD patterns of (a) TiO<sub>2</sub> nanorod arrays, (b) Ag-modified TiO<sub>2</sub> nanorod arrays, (c) TiO<sub>2</sub>/ZnO heterojunction nanotree arrays and (d) Ag-modified TiO<sub>2</sub>/ZnO heterojunction nanotree arrays.



Scheme 1 Schematic diagram of fabrication of Ag-modified TiO<sub>2</sub>/ZnO heterojunction nanotree arrays.



seed layers of TiO<sub>2</sub> nanorod arrays on FTO glass substrates by the dipping-lifting method, pulling and drying every 5 minutes and repeating three times. Finally, it was calcined in a muffle furnace at 480 °C for 1 hour to finally obtain an array of TiO<sub>2</sub> nanorods surrounded by a seed layer of ZnO.

Then, the seed layer is grown into a rod-like structure by hydrothermal method. First, 50 mL of 0.02 mol L<sup>-1</sup> zinc nitrate hexahydrate (Zn(NO<sub>3</sub>)<sub>2</sub>·6H<sub>2</sub>O) and 50 mL of hexamethylenetetramine (C<sub>6</sub>H<sub>12</sub>N<sub>4</sub>) group having a concentration of 0.02 mol L<sup>-1</sup> are prepared. The two solutions were mixed and configured as a growth solution, and the FTO glass substrate coated with the ZnO seed layer coated TiO<sub>2</sub> nanorod array was placed at a 45° angle downward in the reaction vessel, and grown under the environmental condition of 90 °C for four

hours. Finally, a TiO<sub>2</sub>/ZnO heterojunction nanotree arrays is formed on the FTO glass.

## 2.2 Ag-modified TiO<sub>2</sub> nanorod and TiO<sub>2</sub>/ZnO heterojunction nanotree arrays preparation

Ag-modified TiO<sub>2</sub> nanorod arrays and Ag-modified TiO<sub>2</sub>/ZnO heterojunction nanotree arrays were formed by photo-deposition. The TiO<sub>2</sub> nanorod arrays and the TiO<sub>2</sub>/ZnO heterojunction nanotree arrays composite nanostructure FTO substrate were placed in a transparent glass Petri dish, and 30.0 mL of a 0.1 M silver nitrate solution was added and irradiated for 1 hour under ultraviolet irradiation, wherein the color of the sample turns gray. Finally, rinse the surface with deionized water and dry it to obtain the desired sample.

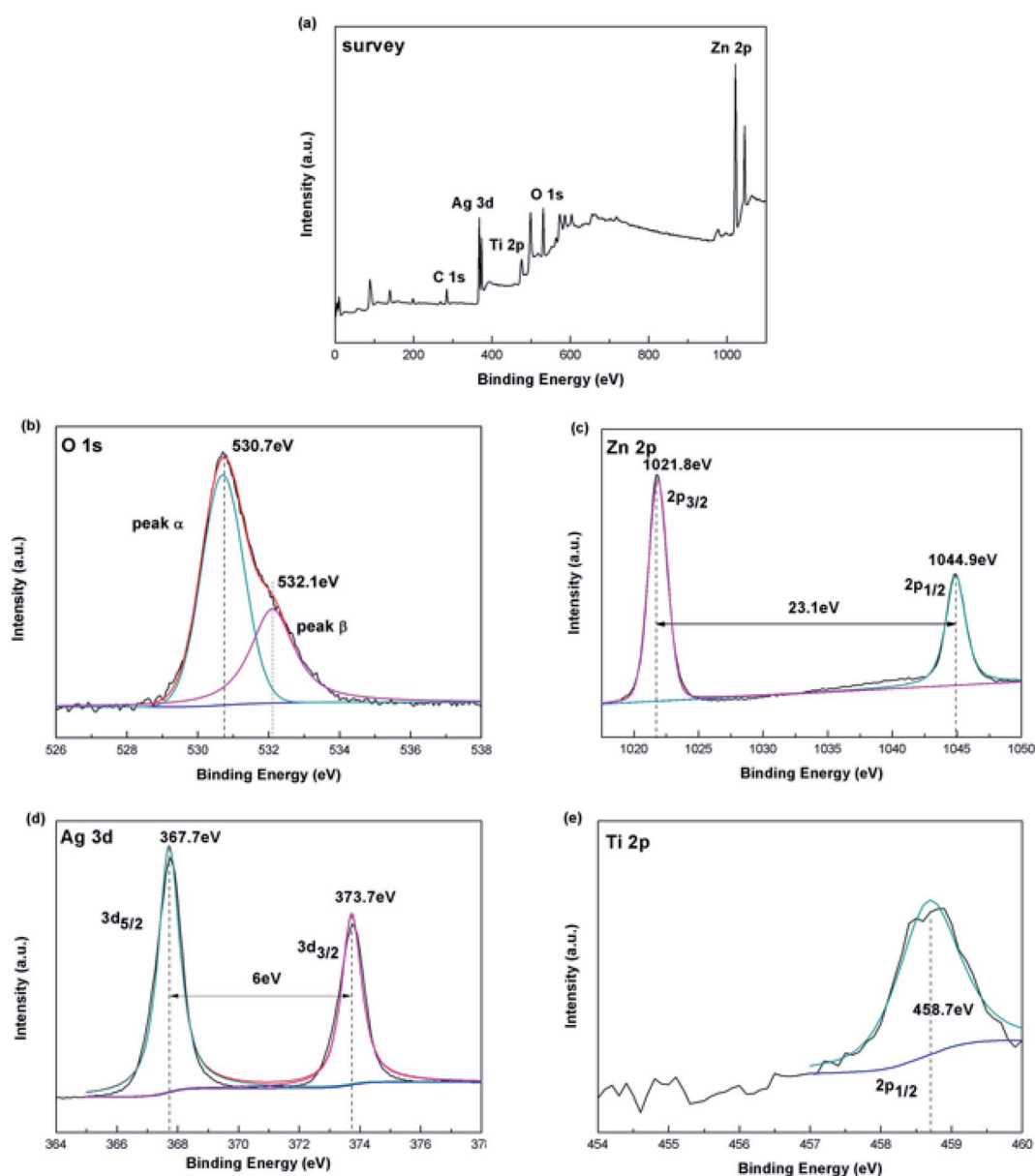


Fig. 2 (a) Survey XPS spectra for Ag-modified TiO<sub>2</sub>/ZnO heterojunction nanotree arrays; (b) O 1s, (c) Zn 2p and (d) Ag 3d (e) Ti 2p XPS high resolution spectrum for Ag-modified TiO<sub>2</sub>/ZnO heterojunction nanotree arrays.



### 2.3 Characterization

The phase composition of the sample was determined using an X-ray diffractometer (XRD MAC, M18XHF) with Cu K $\alpha$  radiation. Scanning electron microscopy (SEM Hitachi, S4800) uses the principle of focused electron beam (1 pA to 2 nA) scanning imaging on the surface of a sample to observe topography. High-resolution transmission electron microscopy (HTEM Hitachi, JEM-2100) uses a very short wavelength electron beam for illumination and an electromagnetic lens for focused imaging to further characterize the topography and physical appearance of the sample. The X-ray photoelectron spectrometer (XPS Thermo, ESCALAB250) uses Al K $\alpha$  as the excitation source and C 1s as the reference peak for calibration to analyze the elemental composition of the sample. The UV-Vis absorption spectrum was measured by a UV-Vis spectrophotometer (UV-2550, Shimadzu). A photoluminescence (PL) spectrum was recorded using a fluorescence spectrophotometer (FL, HITACHI F-4500) under an environmental condition of an excitation wavelength of 325 nm.

### 2.4 Photoelectrochemistry and photocatalytic

The time–current curve of photoelectrochemical properties was measured using an electrochemical workstation in a polysulfide electrolyte (mixed solution of 0.35 M NaSO<sub>3</sub> and 0.25 M NaS) based on a three-electrode system based on a simulated solar source AM 1.5 G and analyzed. The photocatalytic performance test was carried out by disposing 50 mL of 15 mg L<sup>−1</sup> methyl orange (MO) solution as a dye reaction solution under a 15 W ultraviolet lamp with a wavelength range of 200–270 nm. After the photocatalytic reaction was over, the reflection solution was extracted and the light absorption spectrum was measured by a UV-Vis spectrophotometer. Finally, the degradation rate was obtained by using a formula.

## 3. Results and discussion

To ensure that the synthesized film samples have the desired phase composition, the prepared TiO<sub>2</sub> (Curve a), TiO<sub>2</sub>/Ag (Curve b) and TiO<sub>2</sub>/ZnO nano-dendritic heterostructures (Curve c) and Ag-modified TiO<sub>2</sub>/ZnO nano-dendritic heterostructures (Curve d) samples were analyzed by X-ray diffraction. The XRD results are shown in Fig. 1. Analysis of the XRD pattern revealed that the peak of the TiO<sub>2</sub> rutile phase was found at  $2\theta = 36.1^\circ$  [101],  $54.4^\circ$  [211],  $62.7^\circ$  [002],<sup>31</sup> and the peak of the TiO<sub>2</sub> rutile phase corresponding to PDF #21-1276 was well matched. Also in  $2\theta = 31.7^\circ$  [100],  $34.4^\circ$  [002] (the peak of the ZnO wurtzite structure corresponding to PDF #36-1451 is well matched), the presence of ZnO wurtzite structure can be found. However, no diffraction peaks of Ag were found in the map due to the small size of the Ag nanoparticles and the lower than the detection limit of the instrument.<sup>32,33</sup>

To determine the chemical composition and state of the Ag-modified TiO<sub>2</sub>/ZnO nanodendritic structure, we measured its X-ray photoelectron spectroscopy (XPS). The major signals of Zn, O, Ti and Ag are found in survey spectra (Fig. 2(a)). Fig. 2(b)–(e) respectively shows the enhanced energy spectra of O 1s, Zn 2p, Ag

3d and Ti 2p. It can be seen from the enhanced line of Ti 2p (Fig. 2(d)) that the binding energy of Ti 2p is 458.7 eV, corresponding to Ti 2p<sub>3/2</sub>, which proves the existence of Ti<sup>4+</sup>. As shown in Fig. 2(c) there are two peaks were found in the Zn 2p spectrum at 1021.8 eV (Zn 2p<sub>3/2</sub>) and 1044.9 eV (Zn 2p<sub>1/2</sub>). Since in the XPS spectrum no other Zn 2p peaks are observed, the Zn<sup>2+</sup> ions exist as separate ZnO phases.<sup>34</sup> In Fig. 2(c), the nonlinear least-squares fitting procedure will fit the O 1s spectrum to two peaks, corresponding to peak  $\alpha$  and peak  $\beta$ , that means there are two different types of O<sup>2−</sup> in the sample. The low-energy peak at 530.7 eV corresponds to the O<sup>2−</sup> ions in the TiO<sub>2</sub> and the ZnO lattices. The second binding energy of 532.1 eV may be related to surface hydroxyl adsorption of O<sup>2−</sup>. In Fig. 2(d), Ag 3d has two weak peaks with binding energies of 367.7 and 373.7 eV. The energy gap between the two peaks was 6.0 eV, which corresponds to the peak of the metal Ag, showing the presence of Ag element.<sup>35,36</sup>

Scanning electron microscopy (SEM) can characterize the morphology and size of the TiO<sub>2</sub>/ZnO/Ag, TiO<sub>2</sub>, TiO<sub>2</sub>/Ag and TiO<sub>2</sub>/ZnO samples. Fig. 3(a)–(e) is an SEM image of the prepared sample. It can be seen from the Fig. 3(a) that the TiO<sub>2</sub> grown by hydrothermal method grows on the FTO substrate in a rod-like structure. Fig. 3(b) shows the image of Ag QDs on TiO<sub>2</sub> nanorods. The size of Ag NPs obtained by photodeposition has been reported to be 5–15 nm.<sup>37</sup> Fig. 3(c) is an SEM image of ZnO nanoparticles fixed on FTO glass grown from TiO<sub>2</sub> nanorods by sol–gel method, it can be seen from the image that the ZnO nanoparticles are wrapped around the TiO<sub>2</sub> nanorods. The hydrothermal method causes the ZnO particles to grow into a rod-like structure (the Fig. 3(d) can be seen). TiO<sub>2</sub> nanorods

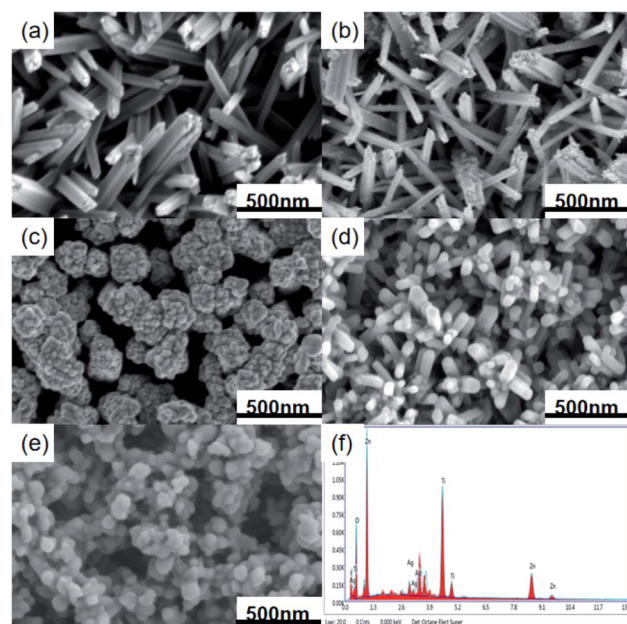


Fig. 3 SEM images of (a) TiO<sub>2</sub> nanorod arrays, (b) Ag-modified TiO<sub>2</sub> nanorod arrays; (c) TiO<sub>2</sub> nanorod arrays/ZnO nanoparticles, (d) TiO<sub>2</sub>/ZnO heterojunction nanotree arrays; (e) Ag-modified TiO<sub>2</sub>/ZnO heterojunction nanotree arrays and (f) an EDS spectrum of Ag-modified TiO<sub>2</sub>/ZnO heterojunction nanotree arrays.





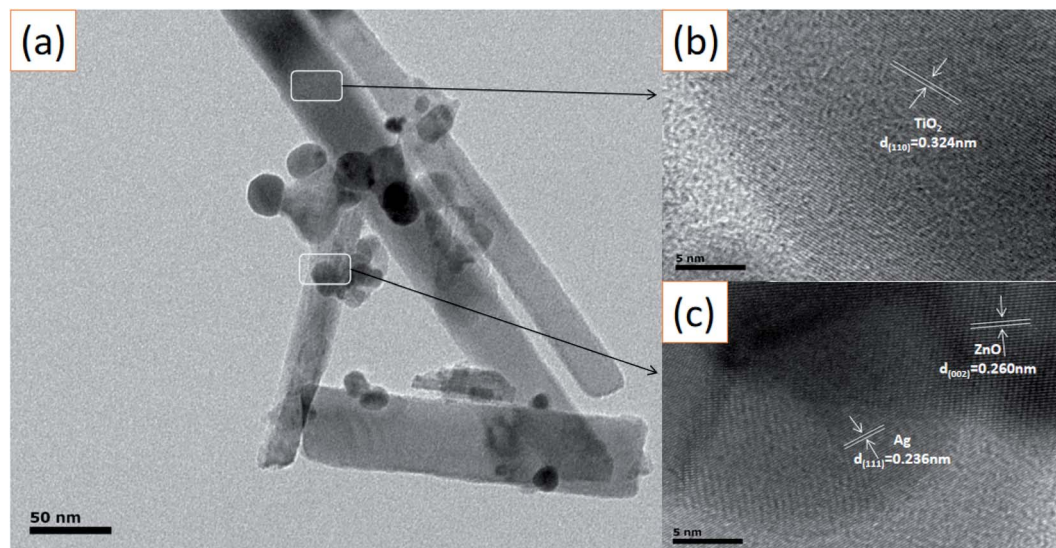


Fig. 4 (a) TEM image of the Ag-modified  $\text{TiO}_2/\text{ZnO}$  heterojunction nanotree arrays; (b) and (c) HRTEM image of the Ag-modified  $\text{TiO}_2/\text{ZnO}$  heterojunction nanotree arrays.

acts as the trunk of the tree, while ZnO nanorods forms the branches of the tree. As shown in Fig. 3(e), Ag QDs were deposited in dendritic ZnO nanorods. Due to the short length of ZnO nanorods, Ag QDs make the dendritic structure less obvious. At the same time, it can be seen from the energy spectrum (Fig. 3(f)) of the Ag-modified  $\text{TiO}_2/\text{ZnO}$  heterojunction nanotree arrays that it contains four elements of Ag, Ti, Zn and O, which is consistent with the results in the X-ray diffraction pattern.

The microscopic morphology of the Ag-modified  $\text{TiO}_2/\text{ZnO}$  heterojunction nanotree arrays sample was further characterized using high-resolution transmission electron microscope (Fig. 4(a)–(c)). The crystal plane having a lattice spacing of 0.32 nm and were ascribed to the (110) crystal plane of the rutile phase  $\text{TiO}_2$ . A series of ordered lattice edges with lattice spacings of 0.260 nm and 0.236 nm can be seen in the branches and belong to the (002) plane of the ZnO and the (111) plane of the

Ag. As can be seen from Fig. 4(a), the diameter of the surface Ag NPs distributed on the ZnO nanorods is about 10–20 nm, which is in agreement with what has been reported in the literature.<sup>37</sup> This can reflect the ZnO nanorods to provide more adhesion area for Ag quantum dots, which will be beneficial to the SPR effect of Ag, photoelectrochemical performance and photocatalytic efficiency.

The optical absorption intensity is the key factors of the photoelectrochemical process. The UV-Vis absorption spectra of different specimens are presented in Fig. 5(a). Pure  $\text{TiO}_2$  exhibits the highest peak at 370 nm due to exciton absorption, and its absorption edge is around 390 nm due to the transfer of charge from the valence band formed by the oxide anion 2p orbital to the conduction band formed by the Ti cation 3d  $t_{2g}$  orbital. Compared with pure  $\text{TiO}_2$ , the red shift of the absorption edge of  $\text{TiO}_2/\text{ZnO}$  heterojunction nanotree arrays is due to the introduction of impurity levels in the forbidden band of

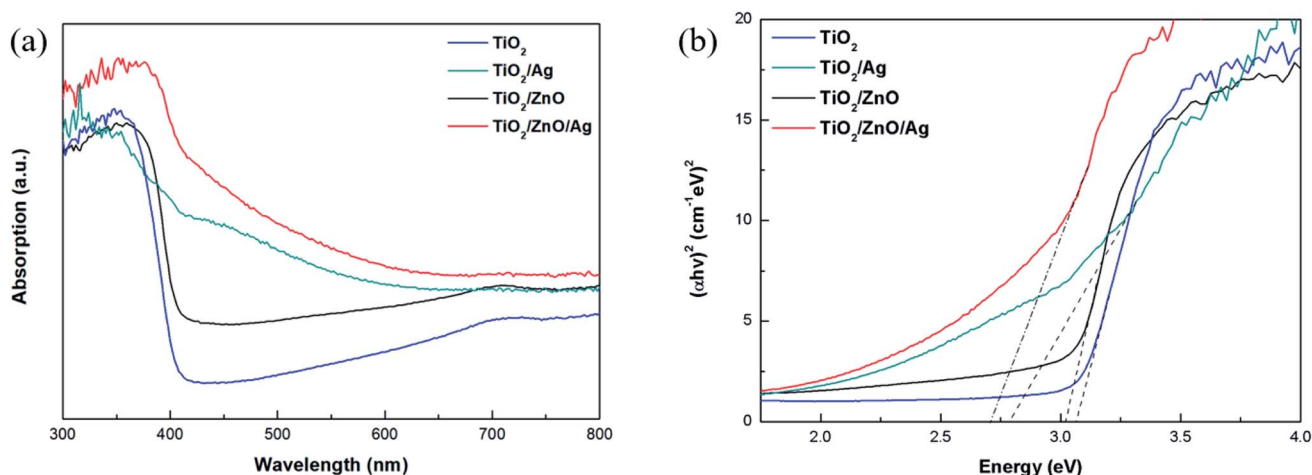


Fig. 5 (a) UV-Vis absorption spectra of various photoelectrodes. (b) Bandgaps of different samples.



TiO<sub>2</sub>, but the red shift phenomenon is not obvious due to the small difference in the forbidden band width of TiO<sub>2</sub> and ZnO. After modification by Ag QDs, the absorption intensity of the sample is enhanced and the absorption is red-shifted because of the LSPR effect produced by the Ag QDs and the presence of electron transitions between the doping element and the base material. Ag NPs have fcc crystal structure and spherical structure. The LSPR wavelength not only depends on the size, shape of the particles, and the dielectric properties of the surrounding medium, but also on interparticle coupling. For Ag nanoparticles with a diameter of 5–15 nm, the LSPR effect is in the range of 430–700 nm.<sup>38–40</sup> Photodeposition can be a method where a large number of Ag NPs are deposited on the sample surface leading to dominant interparticle coupling, which results in absorption of the optical edge redshift. After the introduction of the ZnO intermediate layer, it can be seen that the absorption edge of Ag-modified TiO<sub>2</sub>/ZnO heterojunction nanotree arrays is further red-shifted and the absorption intensity is also increased. At the same time, the direct band gap is shown in Fig. 5(b). It can be seen from the figure that the bandgap width of the TiO<sub>2</sub>/ZnO heterojunction nanotree array is 3.02 eV, which is only slightly reduced compared to pure TiO<sub>2</sub> (3.07 eV). Due to the test environment, instrumentation and light scattering, the TiO<sub>2</sub> bandgap measurements differ from those in the literature.<sup>41–43</sup> The TiO<sub>2</sub>/ZnO bandgap width varies little relative to that of TiO<sub>2</sub>, mainly due to the similar bandgap structures of TiO<sub>2</sub> and ZnO.<sup>44–46</sup> After modification of the Ag quantum dots, the bandgap width was greatly reduced to 2.70 eV for the sample of TiO<sub>2</sub>/ZnO/Ag and 2.78 eV for the sample of TiO<sub>2</sub>/Ag. The reduction of the band gap greatly facilitates light absorption.

Photoluminescence spectroscopy can be used to detect the efficiency of charge transport, capture, transfer and separation. Fig. 6 shows the PL spectra (the excitation wavelength is 325

nm) of TiO<sub>2</sub>, TiO<sub>2</sub>/Ag, TiO<sub>2</sub>/ZnO and TiO<sub>2</sub>/ZnO/Ag prepared at room temperature. It can be seen from the figure that the two main peaks, which is due to photoexcitation caused by TiO<sub>2</sub> edge free exciton recombination and various defects, are located at 452 nm and 469 nm. There are two small peaks at 479 nm and 492 nm due to photoluminescence caused by binding excitons.<sup>47–49</sup> The PL spectrum is mainly due to photo-generated carrier recombination and the lower PL spectrum intensity indicates a decrease in recombination. As can be seen from the figure, the PL spectrum intensity of the Ag-modified TiO<sub>2</sub> nanorod arrays sample is lower than that of the pure TiO<sub>2</sub> nanorod arrays sample. This indicates that the PL spectrum intensity of the Ag-modified TiO<sub>2</sub> nanorod arrays sample has a lower recombination rate than the pure TiO<sub>2</sub> nanorod arrays sample under illumination, because the photogenerated carriers can be captured by the Ag 3d level under the conduction band, thereby inhibiting the recombination. After the introduction of ZnO intermediate layer, the peak of Ag-modified

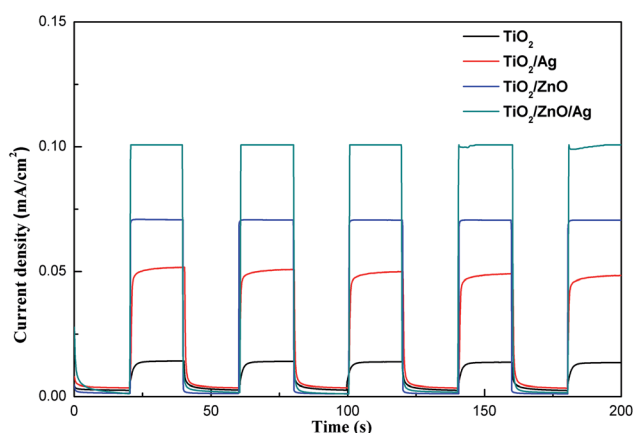


Fig. 7 Transient photocurrent responses of different samples.

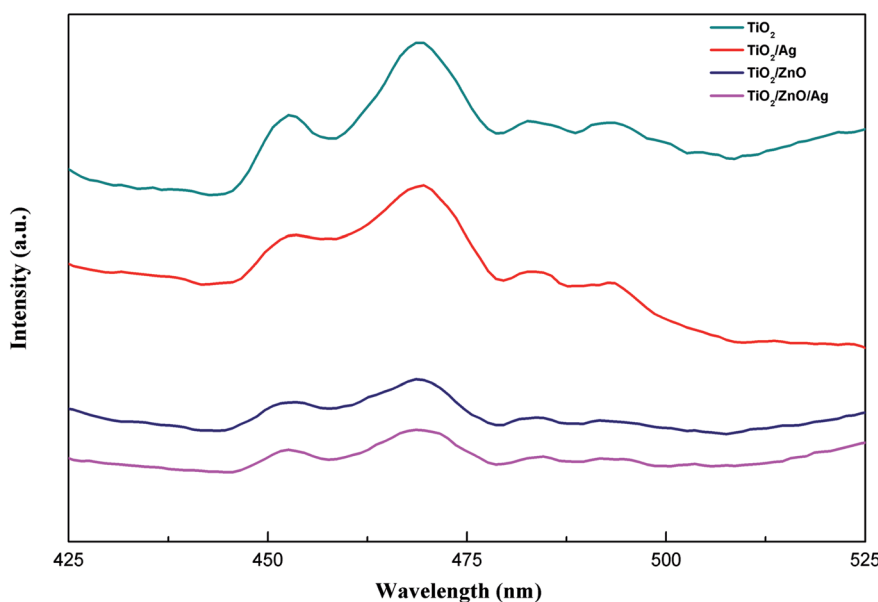


Fig. 6 PL spectra of the samples.



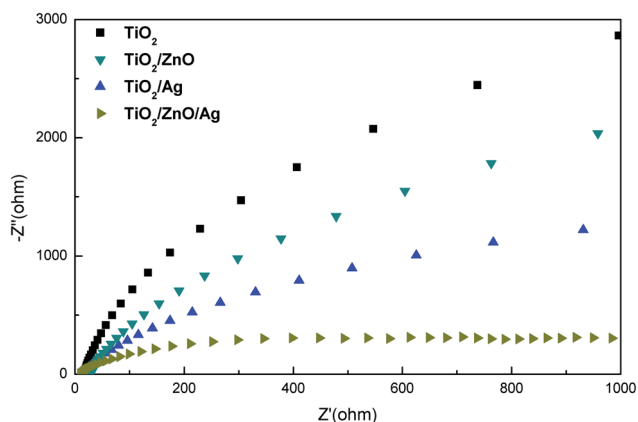


Fig. 8 Electrochemical impedance spectra of all samples.

TiO<sub>2</sub>/ZnO heterojunction nanotree arrays further decreases, indicating that the ZnO intermediate layer makes the recombination rate between photo-generated electron-holes lower and the photoinduced charge carrier recombination is effectively inhibited, thereby improving the photocatalytic activity.

Transient photocurrent testing has long been considered an important evidence for the photoinduced electron-hole transport mechanism of materials. In order to further demonstrate

the photoelectrochemical performance, a transient photocurrent response test was performed. As shown in Fig. 7, the initial photocurrent is soared under transient illumination due to the separation of electron-hole pairs at the semiconductor/electrolyte interface. After reaching the maximum value, the photocurrent will eventually stabilize as time passes. It can be seen from the figure that after 5 turn-on and turn-off cycles, the photocurrent of the sample is relatively stable and exhibits good reproducibility. Under light conditions, the photocurrent of TiO<sub>2</sub>/ZnO heterojunction nanotree arrays is 0.07 mA cm<sup>-2</sup>, which is 5 times that of pure TiO<sub>2</sub> nanorod arrays. The photocurrent of Ag-modified TiO<sub>2</sub> nanorod arrays is doubled compared to pure TiO<sub>2</sub> nanorod arrays, which is 0.047 mA cm<sup>-2</sup>. After introducing the middle layer of ZnO nanorods, the photocurrent reaches 0.1 mA cm<sup>-2</sup>, which is twice that of the Ag-modified TiO<sub>2</sub> nanorod arrays, and even is 8 times that of pure TiO<sub>2</sub> nanorod arrays. It can be proved that the ZnO nanorods as an intermediate layer can contribute to the separation and collection of photoinduced charge carriers.<sup>24</sup>

The method of measuring EIS can be used to verify the charge transport impedance of the sample, the recombination rate of photogenerated electron-hole pairs, and other characteristics. Fig. 8 shows the Nyquist spectra of different samples at 0 V in the dark. At present, it is generally believed that the smaller the radius of curvature of the curve, the smaller the

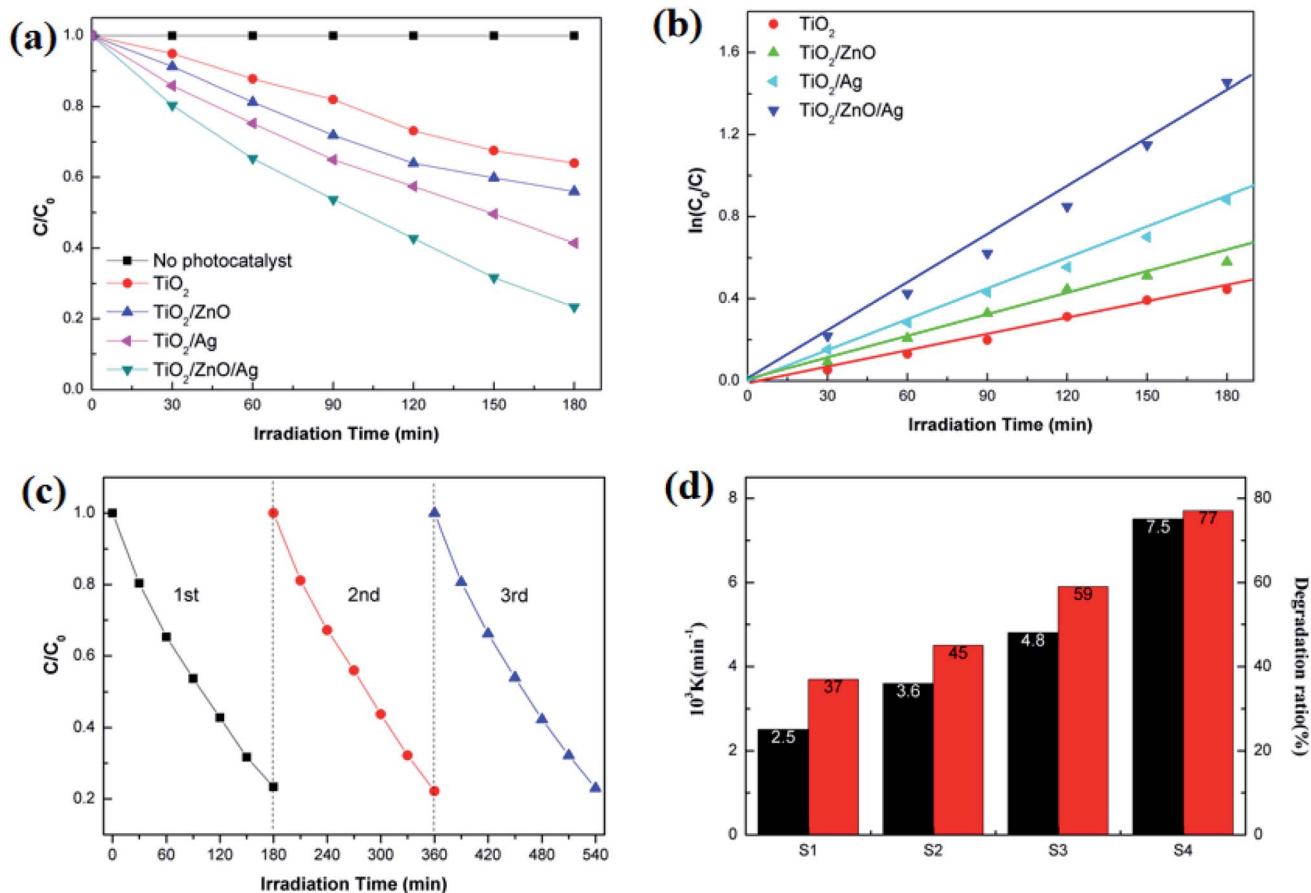


Fig. 9 (a) Photodegradation percentages of different samples for MO; (b) the kinetics of different samples for MO; (c) three successive photodegradation curves for Ag-modified TiO<sub>2</sub>/ZnO heterojunction nanotree arrays; (d) photodegradation ratio and rate constant of S1-S7.



interface charge transfer ability of the sample. From the Fig. 8, it can be observed that the resistance of electrons passing through the interface is the smallest in the Ag-modified TiO<sub>2</sub>/ZnO nanotree array, which shows that the TiO<sub>2</sub>/ZnO nanotree array can effectively reduce the resistance of photogenerated charge transport on the surface and accelerate the transport of photogenerated carriers. This conclusion is consistent with PL analysis.

In order to test the photocatalytic performance, an experiment in which the sample degraded methyl orange (MO) under the solar light source was simulated with an ultraviolet lamp. The Lambert–Beer law and the Langmuir–Hinshelwood model were used to analyze the degradation rate of the sample and the kinetics of degradation of methyl orange to evaluate the photocatalytic efficiency.<sup>50</sup>

$$\eta = \frac{(C_0 - C_t)}{C_0} = \frac{A_0 - A_t}{A_0} \times 100\% \quad (1)$$

$$\ln\left(\frac{C_0}{C_t}\right) = K_d t \quad (2)$$

$\eta$  = degradation rate;  $C_0$  = the initial concentration;  $C_t$  = concentration after reaction time  $t$ ;  $A_0$  = initial absorption luminosity;  $A_t$  = absorption luminosity after reaction time  $t$ ;  $K_d$  = first order rate constant.

As shown in Fig. 9(a), in the case of monitoring the degradation reaction using UV light, it was found that the concentration of MO decreased with the irradiation time. After 180 minutes of exposure to 15 W UV light, the degradation rates of TiO<sub>2</sub> nanorod arrays and Ag-modified TiO<sub>2</sub> nanorod arrays were 37% and 59%. After the introduction of ZnO, the degradation rates of TiO<sub>2</sub>/ZnO and Ag-modified TiO<sub>2</sub>/ZnO were found to be 45% and 77%. It can be seen that the Ag-modified TiO<sub>2</sub>/ZnO heterojunction nanotree arrays showed the highest degradation rate, which was 40% higher than that of the pure TiO<sub>2</sub> nanorod arrays sample and 18% higher than the Ag-modified TiO<sub>2</sub> heterojunction nanotree arrays. It is shown that the Ag-modified TiO<sub>2</sub>/ZnO heterojunction nanotree arrays has high

photocatalytic activity, which is consistent with the results of PL and photocurrent. The linear exchange of pseudo first-order model is used to quantify the reaction kinetics of WO degradation. As shown in Fig. 9(b), it is clear that the slope of Ag-modified TiO<sub>2</sub>/ZnO heterojunction nanotree arrays is the highest, it was shown that the Ag-modified TiO<sub>2</sub>/ZnO heterojunction nanotree arrays had the highest photocatalytic degradation rate constant ( $K_d$ ) and the best photocatalytic activity. Fig. 9(d) shows the photodegradation efficiency constants and photodegradation rates of different samples over 180 min in the form of a histogram, where the numbers S1–S4 represent TiO<sub>2</sub> arrays, TiO<sub>2</sub>/ZnO heterojunction nanotree arrays, Ag-modified TiO<sub>2</sub> arrays and Ag-modified TiO<sub>2</sub>/ZnO heterojunction nanotree arrays. According to the formula, the kinetic constant ( $K_d$ ) bit  $7.5 \times 10^{-3} \text{ min}^{-1}$  of Ag-modified TiO<sub>2</sub>/ZnO heterojunction nanotree arrays can be calculated, which is three times higher than the original TiO<sub>2</sub> ( $2.5 \times 10^{-3} \text{ min}^{-1}$ ). Sample stability was obtained by testing the cyclic stability of the samples through three successive cycles of photodegradation of methyl orange. As shown in Fig. 9(c), methyl orange was stably degraded in all three cyclic reactions, indicating that the sample is an efficient, stable decomposer of organic matter.

Fig. 10(a) is the illustration of the potential and band position in the TiO<sub>2</sub>/ZnO/Ag system, which is based on the work function of the metal Ag (−4.26 eV),<sup>51</sup> the conduction band potentials of TiO<sub>2</sub> (−4.21 eV)<sup>52</sup> and ZnO (−4.05 eV).<sup>46,53</sup> It can be seen that ZnO has the highest conduction band position. Fig. 10(b) is the proposed mechanism of charge-transfer interaction and photodegradation of MO with TiO<sub>2</sub>/ZnO/Ag system. The coupling between the two photocatalysts produces a heterojunction in which ZnO acts as an n-type semiconductor, the electrons are transferred from the conduction band (CB) of ZnO to CB of TiO<sub>2</sub>. In addition, TiO<sub>2</sub> acts as a p-type semiconductor to transfer positive holes from valence band (VB) of TiO<sub>2</sub> to VB of ZnO. Therefore, due to the illumination, the photogenerated holes and electrons produced by pure TiO<sub>2</sub> are very easy to recombine in a short time, but the chance of recombination the of photogenerated electrons and hole charge carriers are greatly reduced because of the conformation of the TiO<sub>2</sub>/ZnO

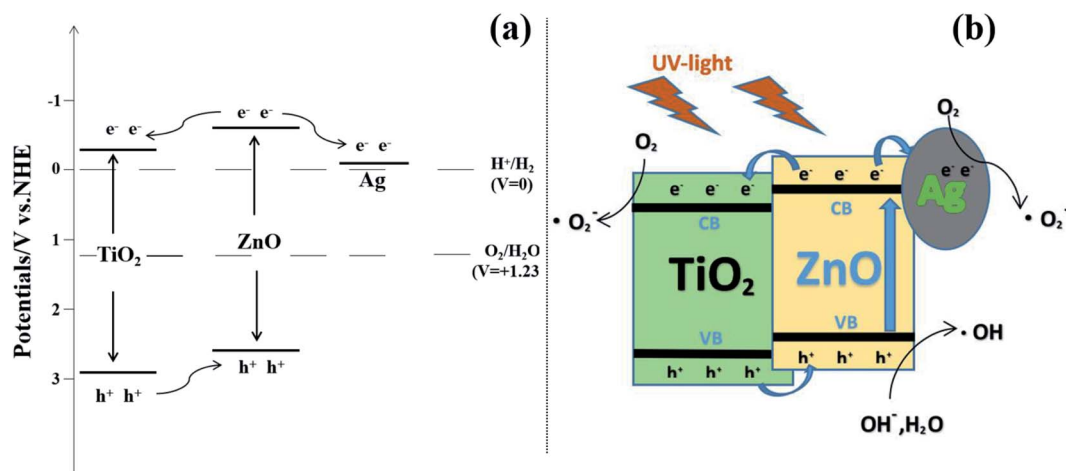
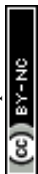
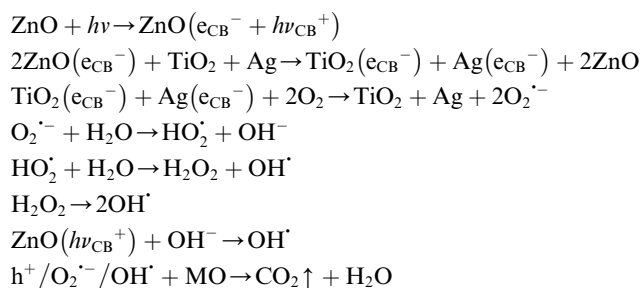


Fig. 10 (a) Illustration of the potential and band position in the Ag-modified TiO<sub>2</sub>/ZnO heterojunction nanotree arrays and (b) proposed mechanism of charge-transfer interaction and photodegradation of MO with TiO<sub>2</sub>/ZnO/Ag system.





heterojunction nanotree arrays. For the case of Ag-modified TiO<sub>2</sub>/ZnO heterojunction nanotree arrays, Ag QDs are deposited on ZnO. The equilibrium Fermi level ( $E_f$ ) of ZnO/Ag heterojunction is lower than the bottom energy level of CB of ZnO.<sup>54,55</sup> Therefore, the photoexcited electrons can be transferred from the CB of the ZnO nanorods to the Fermi level of the metal Ag as the electron trap,<sup>56</sup> thereby effectively promoting the separation of the photo-generated electron-hole. Photogenerated electrons  $e^-$  are captured by O<sub>2</sub> on the surface of TiO<sub>2</sub> and Ag. The electrons and O<sub>2</sub> undergo a reduction reaction to generate reactive oxygen radical O<sub>2</sub><sup>•-</sup>. The  $h^+$  left on the valence band of ZnO will react with H<sub>2</sub>O and produce the sexual oxygen radical OH<sup>•</sup>. So eventually the organic pollutant methyl orange (MO) will be oxidized to CO<sub>2</sub> and H<sub>2</sub>O by  $h^+$ , O<sub>2</sub><sup>•-</sup> and OH<sup>•</sup>.<sup>44,46</sup> In addition, due to the LSPR effect of Ag nanoparticles, the light absorption intensity increases and the absorption edge red shifts. Therefore the sample Ag-modified TiO<sub>2</sub>/ZnO heterojunction nanotree arrays showed good catalytic properties. Taking MO as a class, the important reaction steps in the photodegradation process are summarized as follows:



## 4. Conclusions

The TiO<sub>2</sub>/ZnO heterojunction nanotree arrays was successfully prepared by hydrothermal, sol-gel and secondary hydrothermal method in three steps, and the Ag QDs modification was carried out by photodeposition. The results show that the optical properties, photocatalytic properties and photoelectrochemical performance of Ag-modified TiO<sub>2</sub>/ZnO heterojunction nanotree arrays are improved compared with Ag-modified TiO<sub>2</sub> nanorod array, pure TiO<sub>2</sub> nanorod arrays and TiO<sub>2</sub>/ZnO heterojunction nanotree arrays. Among them, the photocurrent intensity is increased by 8 times and the photocatalytic effect is increased by 40%. In this respect, ZnO has a higher conduction band (VB) than TiO<sub>2</sub> and is more easily excited to produce electrons and the most dendritic structure of ZnO nanorods provides more attachment sites for Ag QDs. On the other hand, because of the distinctive heterostructure of TiO<sub>2</sub>/ZnO, Ag QDs effectively promote the separation of photogenerated electron-hole pairs and the LSPR effect of Ag QDs effectively extend the absorption range of light. In summary, the TiO<sub>2</sub>/ZnO heterojunction nanotree arrays has potential applications in solar cells and photocatalysis.

## Conflicts of interest

There are no conflicts to declare.

## Acknowledgements

This work was successfully completed with the support of the National Natural Science Foundations of China (No. 51772003, 51472003 and 51701001). The authors also would like to thank to Zhongqing Lin and Yonglong Zhuang of the Experimental Technology Center for help with microstructure testing.

## References

- 1 X. B. Chen, S. H. Shen, L. J. Guo and S. S. Mao, *Chem. Rec.*, 2010, **10**, 6503–6570.
- 2 H. J. Li, Y. Zhou, W. G. Tu, J. H. Ye and Z. G. Zou, *Adv. Funct. Mater.*, 2015, **25**, 998–1013.
- 3 L. Y. Hu, Y. M. Zhang and B. X. Li, *RSC Adv.*, 2016, **6**, 43098–43103.
- 4 J. J. Tao, Z. Z. Gong, G. Yao, Y. L. Cheng, M. Zhang, J. G. Lv, S. W. Shi, G. He, X. S. Chen and Z. Q. Sun, *Ceram. Int.*, 2016, **42**, 11716–11723.
- 5 Y. Zhang, J. Zhu, X. Yu, J. Wei and S. Dai, *Sol. Energy*, 2012, **86**, 964–971.
- 6 C. C. Pei and W. W. F. Leung, *Sep. Purif. Technol.*, 2013, **114**, 108–116.
- 7 S. M. Dizaj, F. Lotfipour, M. Barzegar-Jalali, M. H. Zarrintan and K. Adibkia, *Mater. Sci. Eng. C*, 2014, **44**, 278–284.
- 8 S. Parham, D. H. B. Wicaksono, S. Bagherbaigi, S. L. Lee, H. Nur and J. Chin, *J. Chin. Chem. Soc.*, 2016, **63**, 385–393.
- 9 J. M. Wang, C. Li, H. Zhuang and J. H. Zhang, *Food Contr.*, 2013, **34**, 372–377.
- 10 G. Carre, E. Hamon, S. Ennahar, M. Estner, M. C. Lett, P. Horvatovich, J. P. Gies, V. Keller, N. Keller and P. Andre, *Appl. Environ. Microbiol.*, 2014, **80**, 2573–2581.
- 11 A. M. Allahverdiyev, E. S. Abamor, M. Bagirova and M. Rafailovich, *Future Microbiol.*, 2011, **6**, 933–940.
- 12 Y. J. Zou, J. W. Shi, D. D. Ma, Z. Y. Fan, L. Lu and C. M. Niu, *Chem. Eng. J.*, 2017, **322**, 435–444.
- 13 P. Ilanchezhian, G. M. Kumar, F. Xiao, A. Madhankumar, C. Siva, S. U. Yuldashev, H. D. Cho and T. W. Kang, *Sol. Energy Mater. Sol. Cell.*, 2018, **183**, 73–81.
- 14 Z. Y. Hou, Y. X. Zhang, K. R. Deng, Y. Y. Chen, X. J. Li, X. R. Deng, Z. Y. Cheng, H. Z. Lian, C. X. Li and J. Lin, *ACS Nano*, 2015, **9**, 2584–2599.
- 15 J. L. Song, X. Wang and C. C. Wong, *Electrochim. Acta*, 2015, **173**, 834–838.
- 16 J. J. Yin, J. Liu, M. Ehrenshaft, J. E. Roberts, P. P. Fu, R. P. Mason and B. Z. Zhao, *Toxicol. Appl. Pharmacol.*, 2012, **263**, 81–88.
- 17 K. Kolodziejek, J. Sar, K. Wismulek, P. Osewski, M. Warczak, A. Sadkowski, M. Radecka and D. A. Pawlak, *J. Catal.*, 2017, **352**, 93–101.
- 18 A. Chatzitakis, M. Grandcolas, K. Q. Xu, S. Mei, J. Yang, I. J. T. Jensen, C. Simon and T. Norby, *Catal. Today*, 2017, **287**, 161–168.
- 19 R. H. Zha, R. Nadimicherla and X. Guo, *J. Mater. Chem. A*, 2015, **3**, 6565–6573.



- 20 X. Z. Zheng, D. Z. Li, X. F. Li, J. Chen, C. S. Cao, J. L. Fang, J. B. Wang, Y. H. He and Y. Zheng, *Appl. Catal., B*, 2015, **168**, 408–415.
- 21 Y. Wang, H. B. Fang, R. Q. Ye, Y. Z. Zheng and N. Li, *RSC Adv.*, 2016, **6**, 24430–24437.
- 22 F. T. Johra and W. G. Jung, *Appl. Catal. Gen.*, 2015, **491**, 52–57.
- 23 C. A. Huerta-Aguilar, V. Palos-Barba, P. Thangarasu and R. T. Koodali, *Chemosphere*, 2018, **213**, 481–497.
- 24 J. J. Tao, Z. Z. Gong, G. Yao, Y. L. Cheng, M. Zhang, J. G. Lv, S. W. Shi, G. He, X. S. Jiang, X. S. Chen and Z. Q. Sun, *J. Alloys Compd.*, 2016, **688**, 605–612.
- 25 B. Nagaraj and L. G. Devi, *J. Mol. Catal. Chem.*, 2014, **390**, 142–151.
- 26 Q. Sun, Y. Li, X. M. Sun and L. F. Dong, *ACS Sustain. Chem. Eng.*, 2013, **1**, 798–804.
- 27 Z. R. Zheng, H. N. Ji, P. Yu and Z. M. Wang, *Nanoscale Res. Lett.*, 2016, **11**, 266.
- 28 D. H. Yoo, T. V. Cuong, V. H. Luan, N. T. Khoa, E. J. Kim and S. H. Hahn, *J. Phys. Chem. C*, 2012, **116**, 7180–7184.
- 29 H. J. Liang, Z. C. Jia, H. C. Zhang, X. B. Wang and J. J. Wang, *Appl. Surf. Sci.*, 2017, **422**, 1–10.
- 30 T. T. Wang, P. Raghunath, Y. G. Lin and M. C. Lin, *J. Phys. Chem. C*, 2017, **121**, 9681–9690.
- 31 J. J. Tao, M. Zhang, J. G. Lv, S. W. Shi, Z. Z. Gong, G. Yao, Y. L. Cheng, G. He, X. S. Chen and Z. Q. Sun, *Sci. Adv. Mater.*, 2016, **8**, 941–947.
- 32 Z. F. Bian, J. Zhu, S. H. Wang, Y. Cao, X. F. Qian and H. X. Li, *J. Phys. Chem. C*, 2018, **112**, 6258–6262.
- 33 L. Yang, D. L. Chu, Y. Chen, W. H. Wang, Q. H. Zhang, J. H. Yang, M. Zhang, Y. L. Cheng, K. R. Zhu, J. G. Lv, G. He and Z. Q. Sun, *J. Electrochem. Soc.*, 2016, **163**, H180–H185.
- 34 S. Y. Gao, X. X. Jia, S. X. Yang, Z. D. Li and K. Jiang, *J. Solid State Chem.*, 2011, **184**, 764–769.
- 35 C. S. Xing, Y. Zhang, Z. D. Wu, D. L. Jiang and M. Chen, *Dalton Trans.*, 2014, **43**, 2772–2780.
- 36 M. Zhang, G. Yao, Y. L. Cheng, Y. Y. Xu, L. Yang, J. G. Lv, S. W. Shi, X. S. Jiang, G. He, P. H. Wang, X. P. Song and Z. Q. Sun, *Appl. Surf. Sci.*, 2015, **356**, 546–552.
- 37 Y. F. Wang, M. Zhang, L. L. Fang, H. C. Yang, Y. Zuo, J. Gao, G. He and Z. Q. Sun, *J. Am. Ceram. Soc.*, 2019, **102**, 4000–4013.
- 38 T. Ghodselahi, T. Neishaboorynejad and S. Arsalani, *Appl. Surf. Sci.*, 2015, **343**, 194–201.
- 39 J. Borges, C. G. Ferreira, J. P. C. Fernandes, M. S. Rodrigues, M. Proença, M. Apreutesei, E. Alves, N. P. Barradas, C. Moura and F. Vaz, *J. Phys. D Appl. Phys.*, 2018, **51**, 20.
- 40 L. Yang, D. Chu, Y. Chen, W. H. Wang, Q. H. Zhang, J. H. Yang, M. Zhang, Y. L. Cheng, K. R. Zhu, J. G. Lv, G. He and Z. Q. Sun, *J. Electrochem. Soc.*, 2016, **163**, H180–H185.
- 41 M. W. Zhu, G. D. Qian, G. J. Ding, Z. Y. Wang and M. Q. Wang, *Mater. Chem. Phys.*, 2006, **96**, 489–493.
- 42 K. Awazu, M. Fujimaki, C. Rockstuhl, J. Tominaga, H. Murakami, Y. Ohki, N. Yoshida and T. Watanabe, *J. Am. Chem. Soc.*, 2008, **130**, 1676–1680.
- 43 L. L. Fang, X. Z. Wang, Z. Wang, Z. Z. Gong, L. P. Jin, J. Li, M. Zhang, G. He, X. S. Jiang and Z. Q. Sun, *J. Alloys Compd.*, 2018, **730**, 110–118.
- 44 J. P. Wang, Z. Y. Wang, B. B. Huang, Y. D. Ma, Y. Y. Liu, X. Y. Qin, X. Y. Zhang and Y. Dai, *ACS Appl. Mater. Interfaces*, 2012, **4**, 4024–4030.
- 45 Z. K. Zheng, W. Xie, Z. S. Lim, L. You and J. L. Wang, *Sci. Rep.*, 2014, **4**, 5721.
- 46 X. J. Liu, L. K. Pan, T. Lv and Z. Sun, *J. Colloid Interface Sci.*, 2013, **394**, 441–444.
- 47 J. G. Yu, L. F. Qi and M. Jaroniec, *J. Phys. Chem. C*, 2010, **114**, 13118–13125.
- 48 W. F. Zhang, M. S. Zhang, Z. Yin and Q. Chen, *Appl. Phys. B*, 2000, **70**, 261–265.
- 49 M. H. Zhou, J. G. Yu, S. W. Liu, P. C. Zhai and L. Jiang, *J. Hazard. Mater.*, 2008, **154**, 1141–1148.
- 50 R. Georgekutty, M. K. Seery and S. C. Pillai, *J. Phys. Chem. C*, 2008, **112**, 13563–13570.
- 51 P. Gomathisankar, D. Yamamoto, H. Katsumata, T. Suzuki and S. Kaneco, *Int. J. Hydrogen Energy*, 2013, **38**, 5517–5524.
- 52 H. Tong, S. X. Ouyang, Y. P. Bi, N. Umezawa, M. Oshikiri and Y. H. Ye, *Adv. Mater.*, 2012, **24**, 229–251.
- 53 Y. Xu and M. A. A. Schoonen, *Am. Mineral.*, 2000, **85**, 543–556.
- 54 R. Saravanan, M. M. Khan, V. K. Gupta, E. Mosquera, F. Gracia, V. Narayanan and A. Stephen, *J. Colloid Interface Sci.*, 2015, **452**, 126–133.
- 55 P. Madhusudan, Y. Wang, B. N. Chandrashekar, W. J. Wang, J. W. Wang, J. Miao, R. Shi, Y. X. Liang, G. J. Mi and C. Chun, *Appl. Catal. B Environ.*, 2019, **253**, 379–390.
- 56 S. Z. Zhao, Z. Q. Cheng, L. J. Kang, M. T. Li and Z. Gao, *RSC Adv.*, 2017, **7**, 50064–50071.

